PROCEEDINGS, 51st Workshop on Geothermal Reservoir Engineering
Stanford University, Stanford, California, February 9-11, 2026
SGP-TR-230

Modeling Microseismicity in Enhanced Geothermal Systems: Impacts of Injection Parameters at Utah FORGE

Nicolas Cardenas-Acevedo[1], Xu Si[2], Sheng Dai[2], Zhigang Peng[2], Jesse Williams[3], Wencheng Jin[1,*]

[1] Texas A&M University, TX, USA

[2] Georgia Institute of Technology, GA, USA

[3] GTC Analytics, GA, USA

Keywords: Enhanced Geothermal Systems (EGS), Utah FORGE, induced seismicity, hydraulic fracturing, coupled hydro-mechanical simulation.

ABSTRACT

Enhanced Geothermal Systems (EGS) require hydraulic stimulation to increase transmissibility in low-permeability rock formations, such as granites. This process commonly induces microseismicity due to the initiation and propagation of new fractures and slip along pre-existing faults and joints. Understanding the mechanisms and controlling factors of induced seismicity is essential for optimizing stimulation strategies while ensuring operational safety and maintaining public confidence. This study aims to evaluate the influence of key injection parameters on the evolution of microseismicity during hydraulic fracturing stimulation. We develop a series of high-fidelity, hydro-mechanical (HM) numerical simulations with simulation domain replicates stages of the 2024 stimulation performed at well 16A(78)-32 of the FORGE site. Discrete Fracture Network (DFN) was included with fracture hydromechanical properties, such as the aperture, normal stiffness, and friction coefficient, informed by laboratory and borehole observations. The model was calibrated by comparing wellhead pressures and Gutenberg-Richter magnitude-frequency distributions (MFDs) between in situ measurements and numerical predictions. The calibrated model was then employed to quantify the effects of injection rate and inter-stage stress transfer on the maximum magnitude and MFD of induced seismicity during injection. The results show that coupled HM models can reproduce the same induced seismic events statistically during hydraulic fracturing stimulation. For the cases studied, the strong pressure perturbations with sufficient pumping time can produce the highest seismic frequency and larger magnitudes. In contrast, for multistage stimulation, prior nearby injection produces clamping zones on the DFN that reduce seismic event productivity, remarking the importance of accounting for injection history in multi-stage stimulation.

1. INTRODUCTION

The application of hydraulic fracturing on Enhanced Geothermal Systems (EGS) offers a promising pathway to produce clean and renewable geothermal energy from hot rocks that are naturally too tight to circulate fluids efficiently. The connectivity in the reservoir can be increased by opening new fractures and reactivating existing ones. A main uncertainty in this process is induced seismicity caused by a combination of tensile fracture initiation and propagation, as well as shear slip on existing discontinuities. Most events are low in magnitude (microseismicity) and can help map the growth of the reservoir. However, induced seismicity can become a constraint when the project raises concerns about seismic hazards and lacks public acceptance, especially when noticeable events happen near populated areas or when large events occur after shut-in (Majer et al., 2007).

From a physical perspective, induced seismicity results from variations in the in-situ stress state that bring critically stressed fractures and faults to failure. These perturbations are driven by coupled hydro-mechanical processes, such as pore pressure diffusion (effective stress reduction), volume changes (poroelastic stress transfer), stress redistribution (Coulomb static stress changes), aseismic fault slip, temperature changes (thermoelastic effect), chemical alterations, or a combination of them (Boyet et al., 2025; Ge & Saar, 2022). The relative importance of each mechanism depends on the in-situ stress state, the geometry and connectivity of the fractures, and the operational history (e.g., injection and pressure evolution). Consequently, linking injection parameters to the observed evolution of seismicity requires modeling frameworks that explicitly represent the fracture network and account for hydro-mechanical coupling.

The Utah Frontier Observatory for Research in Geothermal Energy (FORGE) provides a unique test site for investigating these relationships because it combines controlled stimulation operations with dense monitoring and well-characterized subsurface conditions. In this study, we focus on the 2024 stimulation conducted at well 16A(78)-32 and use it to assess how injection design affects the microseismic response. Specifically, we examine how the injection rate impacts seismic productivity and magnitude scaling by using a high-fidelity, hydro-mechanical numerical simulator XSite, which uses the lattice method and can model both tensile and shear failures in fractured rock. The models include Discrete Fracture Networks (DFNs) based on site data and are calibrated by aligning observed wellhead pressure and Gutenberg–Richter magnitude-frequency distributions (MFDs). Building on this calibrated baseline, we performed controlled changes to quantify how injection parameters affect the generation of seismicity during stimulation.

2. METHODOLOGY

2.1 The Lattice Method

The coupled hydromechanical simulations were performed using the software XSite. This numerical code is based on the three-dimensional lattice method, which is a simplified version of the bonded particle model (BPM) and the Distinct Element Method (DEM).

The lattice method discretizes the rock as a quasi-random array of nodes connected by normal, shear, and rotational springs that can deform and break when their strengths are exceeded. Spring breakage represents microcrack formation and multiple microcracks can form larger fractures. The mechanical model uses an explicit central difference time integration, which is convenient for strongly non-linear behaviors (fracture creation, propagation, slip, opening and closing). The software calculates the translational and angular degrees of freedom for each node based on the sum of all forces and momentum acting on it. Flow through the fractures is represented using a superimposed network of nodes and pipes. As new microcracks form, this network automatically extends, allowing fully hydromechanical coupling, where fluid pressure reduces effective stress to exacerbate spring breakage, and mechanical deformation simultaneously impacts fluid pressure and permeability (Damjanac et al., 2016).

The numerical code can compute two sources of microseismicity: tensile and shear events. For tensile events, the source is the creation of microcracks when springs in the intact rock matrix fail (forces on the spring reach its bond strength). The event magnitude (M) is calculated using the Hanks & Kanamori (1979) relation:

$$M = \frac{2}{3} logE - 3.2$$

Where E is the radiated seismic energy in Joules, estimated as nearly 1% of the change in strain energy (McGarr et al., 1979).

On the other hand, shear events form due to slip on pre-existing joints. All slips are assumed to be seismic (there is no specific differentiation between seismic and aseismic slip) since there is no slip-weakening on pre-existing fractures in their frictional law. Thus, slip initiates when the shear stress (τ) exceeds frictional resistance, defined by the effective normal stress (σ_n) and the friction angle ($\emptyset$):

$$\tau \geq tan\emptyset\ \sigma_n$$

Once slipping has stopped, the seismic moment (M_o) is calculated based on the shear modulus (G), slip distance (Δu), and area (A):

$$M_o = G\ \Delta u\ A$$

Additionally, the seismic moment is converted into a moment magnitude (M_s) using the relationship (Scholtz, 1990):

$$M_s = \frac{2}{3}\ log\ log\ M_o\ - 6$$

Additionally, the numerical code uses a spatio-temporal clustering algorithm to consolidate individual events that are close together into a macroslip event. The area of contact failure is calibrated using the lattice resolution, and then the software derives a radius for each microslip. If two active microslips occur such that their circular fault areas overlap, they are combined into a single macroslip. When a new microslip is added to an existing cluster, the software updates the total diameter to

$$D = d_i + r_1 + r_2$$

where d_i is the distance between the centers of the combined areas, and r_1 and r_2 are the radii of the fault areas. The clustering is also temporal; when a macroslip is inactive (slip stops), the final moment and moment magnitude are calculated.

2.2 Numerical Model Setup

The numerical simulation represents a granitic reservoir with dimensions of 600 m (length) × 660 m (height) × 600 m (width). Its top boundary is placed at 2050 m depth. The entire domain is rotated 25° relative to the geographic north to align with the principal horizontal stress directions. The fracture network incorporated in the models is represented as hexagonal planes (a convenient geometric approximation of circular joints). The features were identified by rotating the 3D microseismic point cloud from the stimulation of well 16A(78)-32 and visually selecting candidate planes, then refining each plane orientation using a best-fit procedure (Finnila et al., 2023). These discrete features are intended to capture the dominant flow and slip pathways. Fracture sizes span radii from 41.9 to 148.5 m, with hydraulic apertures varying from 22.90 to 60.93 µm across the DFN. In-situ conditions, rock mass, and fracture properties are described in Table 1.

We designed a set of numerical experiments to establish a calibrated baseline and to quantify the seismic response to key injection parameters. The baseline model replicates the FORGE stage 3R re-stimulation from 2024, emulating the pumping schedule using slick water with a viscosity of 2cP, and a maximum pumping rate of 50 bpm during the same time duration as the stimulation performed. This baseline case is validated by comparing simulated wellhead pressure and induced seismicity MFD (Magnitude Frequency Distribution) against field observations. Using the validated baseline as a reference, we then performed controlled parametric variations targeting injection rate, injected volume, fluid viscosity, and injection history.

Table 1. Summary of in-situ stress and pore-pressure gradients, rock-mass properties, and DFN fracture mechanical parameters used in the numerical simulations.

Parameter	Value
In-situ stresses and pore pressure	
Minimum horizontal stress gradient, MPa/m	0.017 – Dip Direction N115°E
Maximum horizontal stress gradient, MPa/m	0.020 – Dip Direction N25°E
Vertical stress gradient, MPa/m	0.026
Pore pressure, MPa/m	0.010
Rock Mass Properties	
Young's modulus, GPa	55
Poisson's ratio	0.26
Tensile Strength, MPa	10
Fracture toughness, MPa.m$^{1/2}$	3
Porosity, %	2
Fracture Properties	
Cohesion, MPa	0
Tensile Strength, MPa	0
Friction Angle, °	37
Dilation Angle, °	2
Normal Stiffness, GPa/m	0.2
Shear Stiffness, GPa/m	0.2

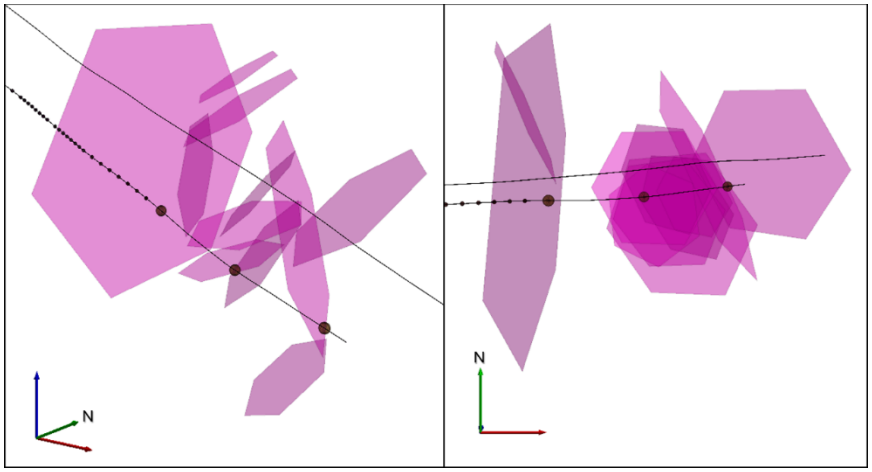

Figure 1. Side (left) and map (right) views of the discrete fracture network (DFN) incorporated in the numerical models, shown relative to the well trajectory within the stimulation domain.

To evaluate the effect of injection rate, we simulated two additional stage 3R scenarios with increased maximum rates of 100 and 150 bpm (double and triple flow rate cases). In these scenarios, the total injected volume is held constant by proportionally adjusting the injection duration. Additionally, to examine the effect of potential injection history and inter-stage stress interactions (stress shadow), we constructed a stage-3R/stage-4 sequence model. In this simulation, the stage 3R model is extended to the shut-in period (3h 59m), and the resulting stress state is transferred as the initial condition for the subsequent stage 4 model. Stage 4 is stimulated using slickwater and a maximum pumping rate of 35 bpm, resembling the pumping schedule performed in 2024. This model is compared against an identical stage 4 stimulation that does not incorporate the stage 3R stress history, allowing us to study the influence of the previous stage stressing with post-injection evolution on stage 4.

3. NUMERICAL RESULTS

3.1. Baseline model behavior and validation

For model validation, we compare the simulated microseismic response of stage 3R against the field observations reported in the Niemz et al., (2025) catalog. That catalog adopts a magnitude threshold of M > −1 for the identified events. Using the same threshold in our analysis, we evaluate whether the numerical model reproduces the pressure evolution and the magnitude–frequency distribution (MFD) of the induced events. Figure 2 summarizes the comparison by showing the injection rate and pressure histories together with the recorded and simulated microseismic events, as well as the corresponding MFDs and magnitude histograms.

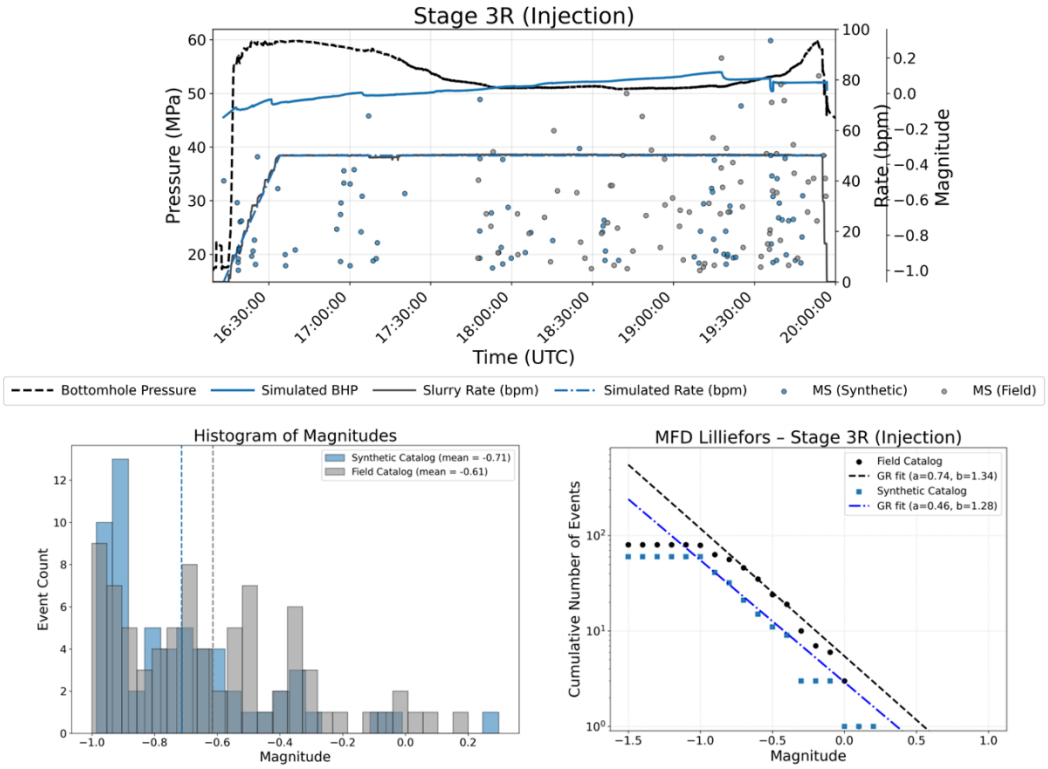

Figure 2. Stage 3R model validation: 1) comparison of injection rate and pressure histories with observed and simulated microseismicity. 2) magnitude histograms. 3) Magnitude Frequency Distribution plots with Gutenberg–Richter parameters.

The pressure match is used as a first-order check that the model captures the coupled hydromechanical loading imposed. We then evaluate whether the model reproduces the statistical and temporal characteristics of the induced seismicity. Initially, the field catalog exhibits a delay between the initiation of pumping and the first detected event, whereas the simulation generates events earlier in the injection. The primary reason for the delay is the aseismic reinflating or refilling of the fractured reservoir, because stages 1-3 were previously stimulated in 2022 and further extended in 2023. From a physical perspective, this behavior is consistent with the Kaiser effect, in which a previously loaded zone deforms with limited seismic emission until stress surpasses a prior maximum state. The current modeling setup does not differentiate seismic from aseismic slip; thus, part of the early deformation that may be aseismic in the field is incorporated as seismic events in the synthetic catalog.

After this onset period, we used a Gutenberg–Richter fit ($log\ N\ = a - bM$), for events above the completeness magnitude, Mc (the minimum magnitude above which all events are reliably recorded). We estimated Mc with a Lilliefors goodness-of-fit test (Lilliefors, 1969), choosing the smallest magnitude for which the remaining larger events do not deviate significantly (significance level α = 0.1). During the injection of Stage 3R, the field catalog contains 80 events (47 events above Mc = -0.70) with a maximum magnitude of 0.20, and the corresponding Gutenberg–Richter parameters are a = 0.7358 and b = 1.3376 ± 0.1394. The synthetic catalog contains 60 events (41 events above Mc = -0.90) with a maximum magnitude of 0.298, and the fitted parameters are a = 0.4637 and b = 1.2779 ± 0.1521. Overall, the simulated and observed MFDs show comparable event productivity above Mc and similar magnitude scaling, supporting the use of the calibrated Stage 3R model as the baseline scenario for subsequent sensitivity studies of injection design.

3.2. Injection Rate Effect

To evaluate the influence of injection rate on the induced seismic response, we performed two additional simulations in which the injection rate was increased to 100 bpm (doubling) and 150 bpm (tripling), while keeping the total injected volume constant with reduced treatment time. Figure 3 shows a systematic increase in simulated bottomhole pressure when increasing the flow rate. Compared to the baseline, the double-rate case reaches a higher plateau, and the triple-rate case attains the steepest and highest pressure. This behavior is consistent with a coupled hydraulic response of a fracture network with finite transmissivity to a larger fluid injection rate. In the numerical code, fracture

flow follows a Poiseuille model with cubic law, so the effective transmissivity depends on the fracture aperture, which evolves as fluid diffuses through the fracture network.

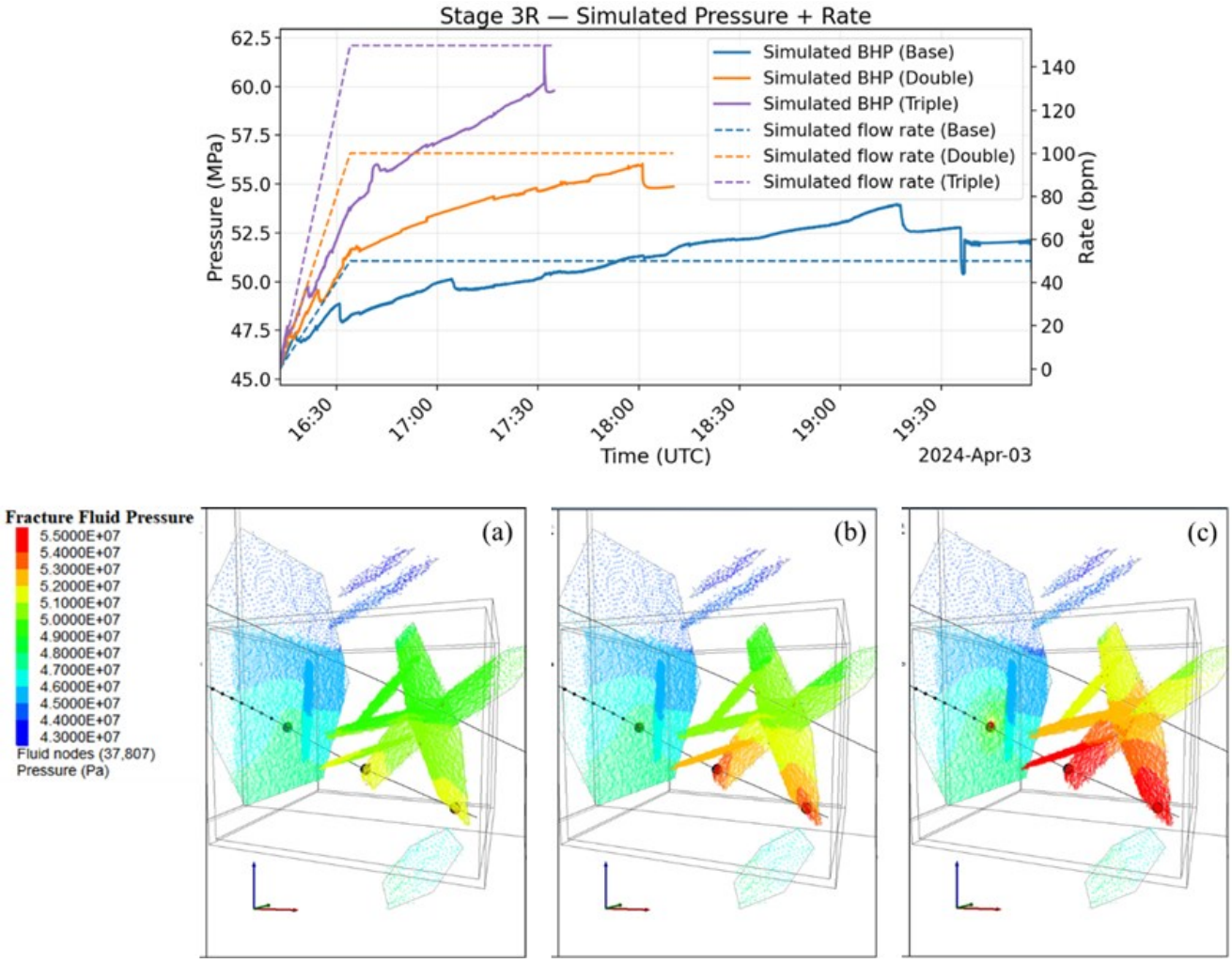

Figure 3. Effect of injection rate on bottomhole pressure and spatial fluid-pressure distribution in the fracture network (stage 3R): (a) base case, (b) double flow rate, and (c) triple flow rate.

The resulting magnitude histograms and frequency distributions (MFDs) in Figure 4 indicate that, during injection, the seismic response strongly depends on the flow rate and pumping duration. The synthetic catalog created for the base case (50 bpm) produced 94 events ($M \geq -1$), with a maximum magnitude of 0.298. Calculating a magnitude of completeness (Mc) of -0.90, 64 events were quantified and resulted in a Gutenberg-Richter fit of a = 0.6216 and b = 1.3174 ± 0.1189. Along with the histogram, this shows that the catalog is dominated by small magnitudes near M = -1. Moreover, doubling the injection rate to 100 bpm significantly increased seismic productivity and moved the distribution toward larger magnitudes. This case contains 444 events (297 events above Mc = -0.80) with a larger M_{max} of 0.765. G-R parameters show a noticeably lower b-value of 0.9565 ± 0.0426, indicating a higher proportion of moderate to larger events, and a-value of 1.7117 consistent with a higher event rate. In contrast, the triple rate case (150 bpm) yields fewer events than the double-rate case, and slightly higher than the base case, with 109 events above M = -1 (M_{max} = 0.671), but with a completeness Mc = 0.0, allowing only 38 events for the G-R fit. This resulted in a large b-value of 1.6949 ± 0.1772, which suggests a rapid decay in larger magnitude events. However, this estimation is relatively uncertain due to the much lower event count from the shorter treatment time.

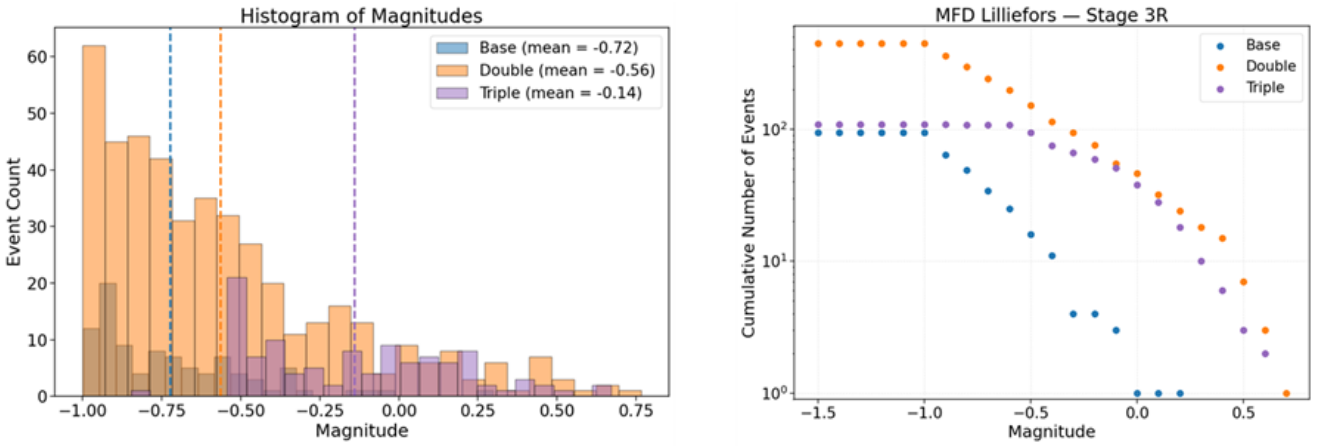

Figure 4. Effect of Injection Rate on (left) magnitude histograms, and (right) magnitude frequency distributions (MFDs).

Figure 5 provides additional insights by separating the stimulated fracture area into tensile and shear components and by distinguishing seismic event types into microcracks (tensile) and slip events (shear) in the magnitude–time plots. The triple-rate case (150 bpm) produces the fastest growth, especially in tensile-stimulated areas. Despite the shorter treatment duration, this scenario generates the largest number of associated tensile seismic events (587 microcracks). However, these events exhibit negligible seismic contribution ($M < -1$), indicating that the rapid tensile expansion is dominated by small-magnitude reactivation and pre-existing fracture extension.

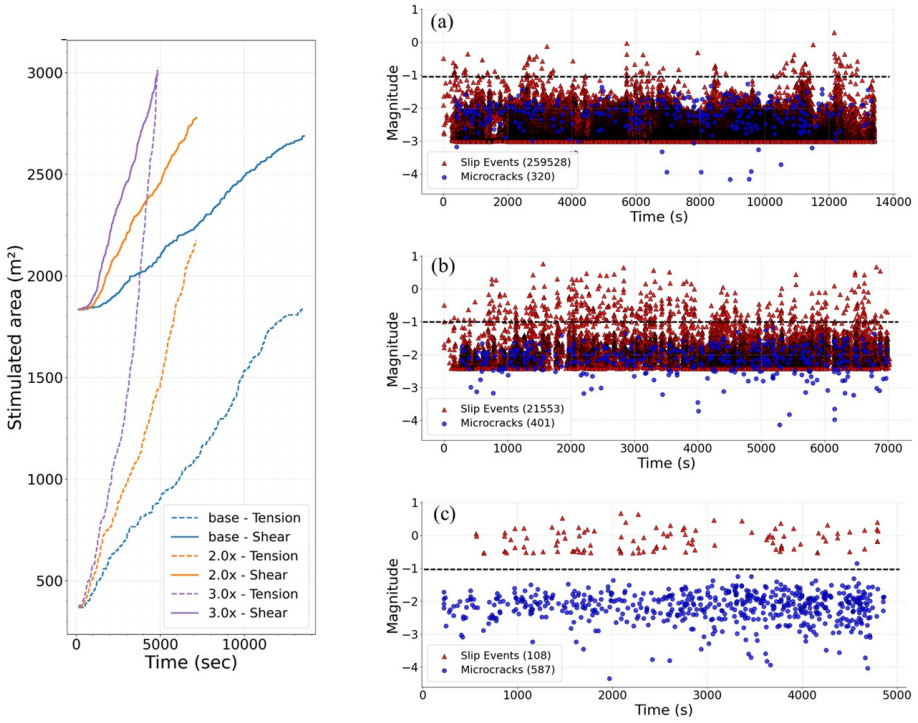

Figure 5. Injection-rate dependence of stimulated fracture area in tension and shear and associated seismicity for (a) base, (b) double and (c) triple flow rate cases.

In contrast, all three injection scenarios develop a fairly similar total area stimulated in shear. As for the number of slip events, it decreases dramatically from 259,528 in the base case to 21,553 in the double-rate case and to only 108 in the triple-rate case. From the Mohr–Coulomb failure perspective, slip initiates once pore pressure reduces the effective normal stress sufficiently to reach the failure envelope. After slipping begins, the seismic moment is governed by slip displacement and the affected area. Because the stimulated shear area is similar across cases, the reduction in event count with increasing flow rate suggests that deformation is accommodated through fewer but faster slip episodes. Higher injection rates impose stronger instantaneous pressure perturbations, leading to more abrupt fracture reactivation within the previously stimulated network. Instead of numerous small slip increments distributed over time, the system accommodates shear displacement more rapidly, concentrating deformation into fewer events. This behavior explains the nonlinear seismic productivity observed in Figure 4. The base case accommodates shear deformation through many small slip events over a longer

duration. The double-rate case combines elevated pressure and sufficient diffusion time, producing both substantial tensile extension and sustained shear activation. The triple-rate case, although generating the highest wellbore pressure and fastest tensile growth, limits the duration of pressure diffusion and therefore reduces the number of shear reactivation events, but with significant magnitude contribution.

3.3. Injection history effect

We simulated stage 4 under two initial conditions to evaluate how a previous stimulation may alter the seismic response. The first model or 'no-history case' is initialized from the regional in-situ stress and pore pressure gradients, and the second one or 'history case' includes local stress changes caused by the simulation of stage 3R following its respective shut-in period (3h 59m). Figure 6 compares the normal stresses on the DFN immediately before the beginning of injection on stage 4. In the no-history case, the normal stress field is relatively smooth and predominantly compressive. In comparison, the 'history' case shows localized zones that are either unclamped (opening) or more strongly clamped (compression). In general, compression increases the traction acting on discontinuities, raising shear resistance and suppressing slip activation, thereby reducing seismic productivity.

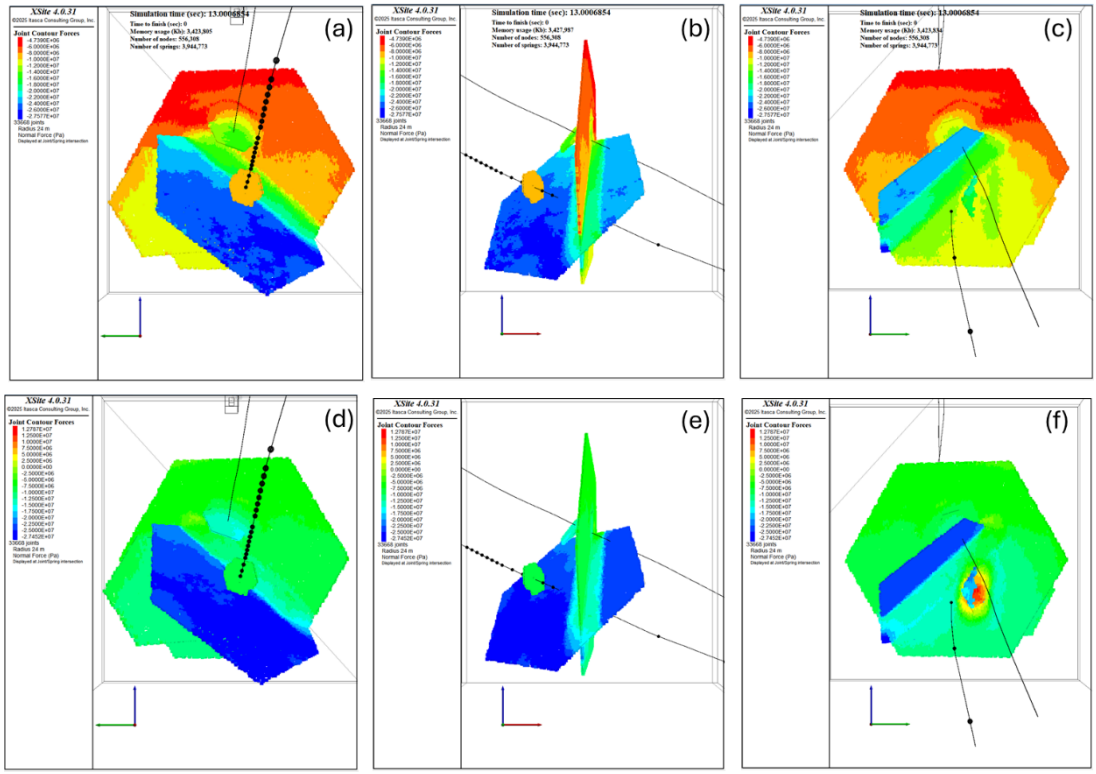

Figure 6. Normal stress distribution on the DFN immediately before injection of stage 4. Top: no-history case. Bottom: history case. Panels show lateral view from W→E (a, d), S→N (b, e) and E→W (c, f).

When looking at the comparison of the simulated bottomhole pressure (Figure 7), it is essentially unchanged despite the modifications in the mechanical state. This suggests that pressure evolution is dictated primarily by the injection schedule (as seen in the flow rate effect cases), and the hydraulic transmissivity of the connected fracture network (Poiseuille model), while the stress perturbation is not large enough to alter the injectivity. In contrast, the seismic response behaves differently. The no-history case produced 83 events above $M \geq -1$, 47 events of which were above $Mc = -0.70$, and with M_{max} of 0.060, whereas the history case was less active with 62 events, 34 of them above the same Mc, and presented a lower M_{max} of -0.185. The Gutenberg-Richter fit for the history case shows a lower a-value of 0.2480, compared to 0.6678, consistent with a reduction in seismic productivity. A steeper b-value of 1.8372 ± 0.2126 on the history case, compared to 1.4375 ± 0.1522, also indicates the prevalence of smaller events in the history case. These events reproduced are smaller in count and magnitude compared to those observed in the field (Niemz et al., 2025) because the model was calibrated using the restimulated stage 3R, which represents a zone in the reservoir that had already been hydraulically conditioned by prior operations. Nevertheless, the comparison of the models demonstrates that localized compressive zones exist during multistage stimulation that suppress slip activation, reducing seismic productivity, lowering the maximum magnitude, and shifting the magnitude distribution toward smaller events. Therefore, for modeling purposes, neglecting injection history can lead to an overestimation of seismicity rates and magnitudes.

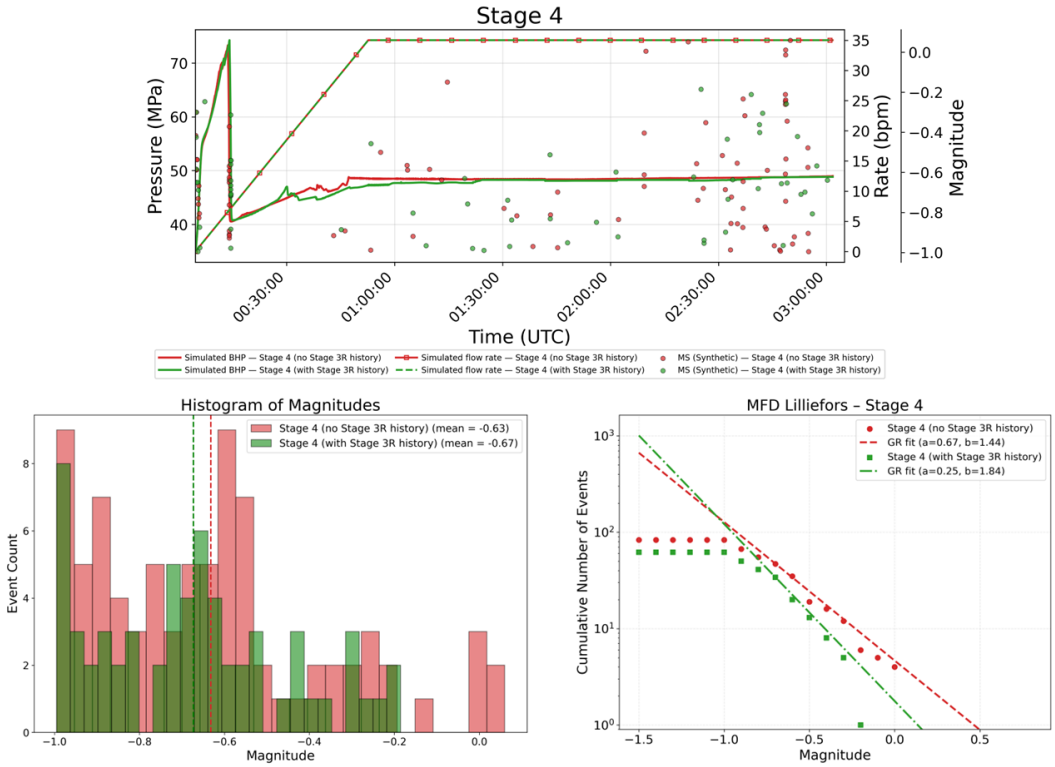

Figure 7. Stage 4 injection history effect – seismic response: 1) simulated pressure and rate histories with corresponding event magnitudes. 2) magnitude histograms. 3) magnitude frequency distributions (MFDs) with Gutenberg–Richter fits.

4. CONCLUSIONS

This study employed a fully coupled hydro-mechanical code with a DFN-based model of the Utah FORGE to quantify how injection design and operational history affect induced microseismicity. The Stage 3R baseline was calibrated against field data to closely match the pressure evolution and reproduce the observed seismic magnitude distribution. The field catalog shows a delayed seismic response with respect to pumping, which is consistent with early aseismic deformation in a previously stimulated region of the reservoir; in contrast, the model produced earlier events because it did not distinguish between seismic and aseismic slip.

A flow rate test at constant injected volume demonstrated how increasing the pumping rate systematically elevated the simulated bottomhole pressure. However, the change in the seismic response was not linear. The 100-bpm case produced a substantially larger number of events than both the highest flow rate (150 bpm) and the longer duration cases (50 bpm), as well as the highest magnitudes. The increased near-wellbore pressure led to an earlier and stronger effective stress drop, and when combined with long enough treatment time, allowed pressurized fluid to propagate further into the reservoir, thereby, generating increased seismic activity.

The analysis of injection history showed that stimulation of a prior stage could suppress seismicity without altering injectivity. Stress transfer from Stage 3R into Stage 4 produced localized compressive normal stress on nearby fractures (i.e., a stress shadow), thereby increasing effective normal traction and suppressing slip. Pressure histories remained nearly identical, but the 'history' case showed fewer events, a smaller maximum magnitude, a lower a-value, and a higher b-value.

Overall, the results highlighted that seismic hazard is controlled not only by injection rate and pressure response, but also by the evolving mechanical state of the fracture network and inter-stage stress interactions.

ACKNOWLEDGEMENT

Funding for this work was provided by the U.S. DOE under grant DE-EE0007080 "Probabilistic Estimation of Seismic Response Using Physics-Informed Recurrent Neural Networks". This research made use of the resources of Texas A&M High Performance Research Computing is appreciated.

REFERENCES

Damjanac, B., Detournay, C., & Cundall, P. A. (2016). Application of particle and lattice codes to simulation of hydraulic fracturing. *Computational Particle Mechanics*, *3*(2), 249–261. https://doi.org/10.1007/s40571-015-0085-0

Finnila, A., Damjanac, B., & Podgorney, R. (2023). *Development of a Discrete Fracture Network Model for Utah FORGE using Microseismic Data Collected During Stimulation of Well 16A(78)-32*.

Gaucher, E., Schoenball, M., Heidbach, O., Zang, A., Fokker, P., Van Wees, J.-D., & Kohl, T. (2015). Induced Seismicity in Geothermal Reservoirs: Physical Processes and Key Parameters. In *Proceedings World Geothermal Congress*.

Hanks, T. C., & Kanamori, H. (1979). A moment magnitude scale. *Journal of Geophysical Research B: Solid Earth*, *84*(B5), 2348–2350. https://doi.org/10.1029/JB084iB05p02348

Lilliefors, H. W. (1969). On the Kolmogorov-Smirnov Test for the Exponential Distribution with Mean Unknown. *Journal of the American Statistical Association*, *64*(325), 387–389. https://doi.org/10.1080/01621459.1969.10500983

Majer, E. L., Baria, R., Stark, M., Oates, S., Bommer, J., Smith, B., & Asanuma, H. (2007). Induced seismicity associated with Enhanced Geothermal Systems. *Geothermics*, *36*(3), 185–222. https://doi.org/10.1016/j.geothermics.2007.03.003

McGarr, A., S. Spottiswoode, N. Gay and W. Ortlepp. (1979) "Observations Relevant to Seismic Driving Stress, Stress Drop, and Efficiency," J. Geophys. Res., 84(B5), 2251–2261

Niemz, P., Pankow, K., Isken, M. P., Whidden, K., McLennan, J., & Moore, J. (2025). Mapping Fracture Zones with Nodal Geophone Patches: Insights from Induced Microseismicity During the 2024 Stimulations at Utah FORGE. *Seismological Research Letters*, *96*(3), 1603–1618. https://doi.org/10.1785/0220240300

Scholtz, C. H. (1990) The Mechanics of Earthquakes and Faulting. Cambridge: Cambridge University Press.